Goudarz Ghanizadeh Hesar, Yeliz Pekbey*, Hasan Yildiz and Farshid Khosravi Maleiki

# A mesh-free simulation of mode I delamination of composite structures

**Abstract:** A numerical and experimental investigation for the analysis of delamination problem under mode I loading in composite material is presented. Firstly, the simulation of the delamination under mode I loading and failure of composite materials based on the cohesive segments model is investigated by using the meshfree method. With the partition of unity of moving least-squares shape functions, the discontinuities at the cohesive segments are approximated with additional degrees of freedom at the nodes. An iterative solution scheme between the continuous and discontinuous fields is presented to solve mode I delamination growth. Secondly, to verify the meshfree method's results, an experimental investigation and the finite element method were used for the simulation of delamination. The experimental study used a double-cantilever beam made of carbon/epoxy laminate (AS4/3501-6) which consists of 10 plies in $[0]_{10}$ and $[0/90/0/90/0]_s$ layup with delamination inserted in the middle of the laminate. The critical fracture force, which can be experimentally measured, was used to calculate the mode I delamination fracture toughness of the carbon/epoxy laminate. Results obtained from the meshfree method showed very good agreement with experimental data for single-mode delamination under mode I loading. The meshfree method could also be used effectively to produce delamination growth in composite laminates and is especially suitable for the simulation of complex delamination patterns that are difficult to model using traditional numerical methods.

**Keywords:** delamination; double cantilever beam; element free Galerkin method; energy release rate; meshfree modeling; mode I loading; moving least squares.

***Corresponding author: Yeliz Pekbey,** Ege University Department of Mechanical Engineering, Izmir, Turkey,
e-mail: pekbey.yeliz@gmail.com
**Goudarz Ghanizadeh Hesar, Hasan Yildiz and Farshid Khosravi Maleiki:** Ege University Department of Mechanical Engineering, Izmir, Turkey

## 1 Introduction

Composite materials are ideal for structural applications where high strength-to-weight and stiffness-to-weight ratios are required. Structural collapse in a composite structure is brought about by the evolution of different types of damage mechanisms, such as fiber fracture, matrix transverse cracking, and delamination. The particular damage modes are based on loading, geometry, layup, and stacking sequence. One of the most common types of damage in laminated fiber-reinforced composites is delamination which refers to debonding of the layers. The presence and the growth of delamination in laminates considerably reduce the compressive load-carrying capacity of a structure and bring about initiation of catastrophic failure. Therefore, the issue of delamination failure is very important when designing composite structures.

In the case of transverse concentrated loads caused by low velocity impacts, delamination may occur. This damage mode is especially important for the structural integrity of composite structures since it is difficult to detect during inspection. Moreover, delamination creates a drastic reduction of the bending stiffness of a composite structure and, when compressive loads are present, supports local buckling [1].

In order to use the full capacity of a composite structure, it is important that the initiation of delamination cracks and the resulting reduction in laminate strength can be correctly modeled. Predicting whether the delamination will grow as the structure is loaded is particularly interesting.

Simulation of these events is crucial but still quite complicated. The simulation of delamination in composites is usually divided into delamination initiation and delamination propagation. Delamination initiation is usually based on the mechanics of materials theory and uses stress criteria normally based on point or average stress, but delamination propagation is modeled with fracture mechanics tools which rely on the evaluation of the strain energy release rate $G$ [2]. Delamination growth is estimated when a combination of the components of the energy release rate is equal to a critical value. It is assumed that when the energy release rate, $G$, exceeds the critical value and the critical energy release rate, $G_c$, delamination grows. In fracture mechanics approach to delamination problems in composites, the strain energy release rate ($G$) is often appraised because of an experimentally measurable quantity and it has been mathematically well defined. The calculation of the strain energy release rate was based on the stiffness loss due to delamination,

calculated by means of the classical laminate theory. The value of the critical energy release rate, $G_C$ ($G_{IC}$, $G$, $G_{IIIC}$), is used for the characterization of interlaminar fracture toughness of composites.

Computational methods such as the finite differences method, the finite element method, or the finite volume method all make use of a mesh, i.e., a set of nodes with node-to-node connectivity which have received much attention over the last 10 years. Since these methods have been successfully used to solve engineering problems for decades, some limitations of these kinds of methods are becoming more and more obvious: mesh generation is very time consuming, and, in problems with moving boundaries, a drastic loss of accuracy is observed due to the distortion of the elements. Therefore there is a need to develop meshfree (grid-free, mesh-less) methods that do not suffer from the problems described above.

In the meshfree method, discontinuities are not restricted to element boundaries or even no elements are necessary at all. Only nodes are used for approximation. The method uses a set of nodes dispersed within the problem domain along a set of nodes dispersed on the boundaries of the domain to represent the problem domain and its boundaries. These sets of scattered nodes are called field nodes, and they do not form a mesh, meaning they do not require any *a priori* information on the relationship between the nodes for the interpolation or approximation of the unknown functions of field variables. For more details, one should refer to Fries and Matthies [3] and Liu [4, 5]. A detailed discussion of mesh free methods, how they work, how to use and develop one, as well as the problems associated with the element-free methods can be done. Also, in Refs. [3–6], meshless application to various mechanics problems such as mechanics for solids (two-dimensional solids), mechanics for structures (beams, plates, and shells), and fluid mechanics is given. Several review articles [6–18], which cover the classification, application, and computer implementation aspects of the meshfree method, have been reported in the literature.

The element-free Galerkin method (EFGM) is one of the most powerful meshfree methods. At the same time, some works have been reported using this method, the meshfree cohesive segment method, or a meshfree penalty approach [2, 19]. Meshfree methods have been around for a number of years, and the EFGM was first proposed for the simulation of fracture 15 years ago, Belytschko et al. [20, 21]. Belytschko et al. [21] presented an overview of meshless methods, focusing on three themes: kernel approximations, moving least squares, and partitions of unity. Each theme provides a different viewpoint for constructing meshless approximations which are constructed by kernel methods, and moving least squares are identical once the requirement of consistency is imposed.

Meshfree methods and the application of composite fracture are still in use in in-depth research. Meshfree methods are very widely used for modeling problems with moving boundaries such as crack growth in solids, because changing discontinuities can be displayed very easily by modifying only the weighting functions which is a well-known advantage compared to the classical finite element method [22].

Many researchers have studied the effect of delamination on the load-carrying capacity of composites experimentally, analytically, and using the finite element method.

This study presents a meshfree method for the simulation of delamination and failure of composite materials based on the cohesive segments model. With the partition of unity of moving least-squares (MLS) shape functions, the discontinuities at the cohesive segments can be approximated with additional degrees of freedom of the nodes. An iterative solution scheme between the continuous and discontinuous fields is presented to solve the mode I delamination growth problem.

A model for the simulation of delamination under mode I loading was developed in this paper. A numerical solution and an experimental investigation for the analysis of delamination problem under mode I loading in composite materials are presented. Firstly, a meshfree method is presented for the simulation of the delamination under mode I loading and failure of composite materials based on the cohesive segments model. The problem is solved for $[0]_{10}$, $[0/45/\text{-}45/90/0]_s$, $[0/90/0/90/0]_s$, $[0/90/0/90/30]_s$, $[0/90/0/90/45]_s$, and $[0/90/0/90/60]_s$ laminates with mid-plane delaminations, and the results are verified for different composite materials. Secondly, experimental investigation and the finite element method are used for the simulation of delamination. The experimental study considered a double-cantilever beam (DCB) made of carbon/epoxy laminate (AS4/3501-6) which consists of 10 plies in $[0]_{10}$ and $[0/90/0/90/0]_s$ layups with artificially embedded delaminations after 5 plies from the upper surface. The critical fracture force, which can be measured experimentally, was used to calculate the mode I delamination fracture toughness for carbon/epoxy laminate. The critical fracture force, $P_c$, which can be measured experimentally, was used to calculate the mode I loading delamination fracture toughness, $G_{IC}$. Finally, the numerical predictions obtained from meshfree and finite element methods are compared with experimental results.

## 2 The meshfree method

A number of different meshfree methods have been developed. One of the most widely used is the EFGM. The EFGM is a method that implements the connectivity between the nodes and sets completely the approximation functions. The EFGM uses the MLS approximants in order to obtain test and trial functions, background cells are utilized for numerical integration in the weak form, and essential boundary conditions are implemented using Lagrange multipliers. The weak form of Galerkin is used to develop the discretized system of equations [4, 5].

The meshfree method is described in a broad sense as a method where nodes are not required to be interconnected. A distribution of nodes is generated to define the domain and its boundaries, and the solution of the problem is sought at these nodes in the EFGM. However, cells are also prescribed over the domain and used for numerical integration. In the element-free Galerkin approach, the MLS scheme is utilized for interpolation, and a mesh of background cells, with no required connection to the nodal discretization, is used for the purpose of numerical integration [15, 16].

### 2.1 The moving least squares shape functions

The moving least squares interpolation is one of the important data-fitting techniques that are the basis of EFGM's formulation. In this scheme, the least squares measure of the error is weighted to create a favorable bias for the neighborhood of the current function evaluation [16].

Consider an unknown scalar function of a field variable $u(x)$ in the domain, Ω, where Ω is the entire domain. The EFGM uses the moving least-squares approximants in order to obtain the function $u^h(x)$, the approximation of the displacement field of the function $u(x)$, and the real displacement field. The approximation $u^h(x)$ of the function $u(x)$ is defined in the domain Ω as

$$u^h(x)=\sum_{j=1}^{m} P_j(x)a_j(x)=P^{\mathrm{T}}(x)a(x) \tag{1}$$

and $P_j(x)$, $j$=1, 2, ..., $m$ are monomial basis functions, $m$ is the number of terms in the basis, and $a_j(x)$ are the coefficients of the basis functions. $u^h(x)$ is also defined as a moving least-square interpolant of a generic function $u(x)$ [12]. Examples of commonly used bases are in one dimension [20, 21]

$$\boldsymbol{P}^{\mathrm{T}}=(1, x) \tag{2}$$

and in two dimensions

$$\boldsymbol{P}^{\mathrm{T}}=(1, x, y) \quad \text{linear basis} \tag{3a}$$

$$\boldsymbol{P}^{\mathrm{T}}=(1, x, y, x^2, xy, y^2) \quad \text{quadratic basis} \tag{3b}$$

$$\boldsymbol{P}^{\mathrm{T}}=(1, x, y, x^2, xy, y^2, x^3, x^2y, xy^2, y^3) \quad \text{cubic basis.} \tag{3c}$$

The coefficients $a(x)$ are functions of $x$ and are indicated as

$$a(x)=\{a_1(x), a_2(x), ..., a_m(x)\} \tag{4}$$

These coefficients are obtained at any point $x$, minimizing the weighted discrete norm $J$,

$$J=\sum_{i=1}^{n}\hat{W}(x-x_i)\left[P^{\mathrm{T}}(x_i)a(x)-u_i\right]^2 \tag{5}$$

where $n$ is the number of nodes in the domain of influence of $x$ for which the weight function $\hat{W}(x-x_i)\neq 0$ and $u_i$ refers to the nodal parameter of $u$ at $x=x_i$. The kernel $\hat{W}(x-x_i)$ or weight function ensures the interpolation of compactness and also controls the degree of continuity of the resulting MLS interpolation. The cubic spline weight function, quadratic spline function, and exponential function are generally used as a weight function in the one-dimensional case. Some common choices of the weight functions are listed in Table 1, in which $\alpha$ is a constant of the shape parameter. The choice of the weight function is important since it is effective in ensuring the continuity of the shape functions. It must be a positive function that guarantees a unique solution for $a(x)$.

The final MLS approximation can be obtained with the solution of $a(x)$ [17]:

$$u^h(x)=\sum_{i}^{n}\phi_i(x)u_i \tag{6}$$

**Table 1** Some possible weight functions in the EFGM.

| Weight function | Expression |
|---|---|
| Cubic spline | $\hat{W}_i(x)=\begin{cases} 2/3-4\bar{r}_i^2+4\bar{r}_i^3 & \bar{r}_i\le 0.5 \\ 4/3-4\bar{r}_i+4\bar{r}_i^2-4/3\bar{r}_i^3 & 0.5<\bar{r}_i\le 1 \\ 0 & \bar{r}_i>1 \end{cases}$ |
| Quadratic spline | $\hat{W}_i(x)=\begin{cases} 1-6\bar{r}_i^2+8\bar{r}_i^3-3\bar{r}_i^4 & \bar{r}_i\le 1 \\ 0 & \bar{r}_i>1 \end{cases}$ |
| Exponential | $\hat{W}_i(x)=\begin{cases} e_i^{-(\bar{r}_i/\alpha)^2} & \bar{r}_i\le 1 \\ 0 & \bar{r}_i>1 \end{cases}$ |
| $\bar{r}_i=\frac{d_i}{d_s}=\frac{\sqrt{(x-x_i)^2+(y-y_i)^2}}{d_s}$ | |

$$u^h_{(2\times1)}=\begin{Bmatrix}u\\v\end{Bmatrix}=\begin{bmatrix}\phi_1 & 0 & \dots & \phi_n & 0\\ 0 & \phi_1 & \dots & 0 & \phi_n\end{bmatrix}\begin{Bmatrix}u_1\\v_1\\\vdots\\u_n\\v_n\end{Bmatrix}=\Phi_{(2\times2n)}u_{(2n\times1)} \quad (7)$$

where $\phi_i(x)$ is the shape function and $n$ is the number of nodes with domains of influence containing the point $x$. The shape functions constructed with respect to MLS have compact support, or domain of influence, which is identical to the support of the corresponding weight function. The support can be of arbitrary shapes, such as circular, rectangular, and square. The two popular types of supports contain the circular and rectangular.

## 3 Cohesive zone model approach

One of the most commonly used tools to investigate interfacial fracture is the cohesive zone model approach. The cohesive zone model is used to model material discontinuities. Consider a domain Ω containing a material discontinuity, $\Gamma_c$ which divides the domain Ω into two parts, $\Omega_1$ and, under crack, $\Omega_2$, as shown in Figure 1 [2]. The stress field inside the domain, $\sigma$, is related to the external loading and to the closing tractions in the material discontinuity through the equilibrium equations. The solid can be loaded by body force $b$ and surface traction (force) $t$ in any distributed fashion in the volume of the solid and the traction $\tau(v)$ in the boundary $\Gamma_c$.

The traction $\tau$ depends on the displacement jump $v$ on the cohesive segment $\Gamma_c$. If $u_1(x)$ is the displacement of sub-domain $\Omega_1$ and $u_2(x)$ is the displacement of sub-domain $\Omega_2$, the displacement jump $v(x)$ is expressed as follows:

$$v(x)=u_1(x)-u_2(x) \quad \text{on } \Gamma_c \quad (8)$$

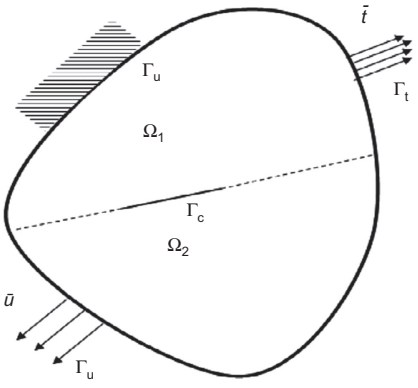



**Figure 1** Body Ω involving discontinuity caused by two cohesive segments.

Cohesive damage zone models relate cohesive surface tractions, $\tau$, to displacement jumps, $v$, at an interface where a crack may occur. The bi-linear constitutive relationship, shown in Figure 2, is often used [1, 2]:
where $v_o$ is the onset displacement jump and $v_f$ is the final displacement jump. The initial damage threshold is obtained from the formulation of the initial damage surface or initial damage criterion. The final displacement jump is obtained from the formulation of the propagation surface or propagation criterion. The criteria used to predict delamination propagation are usually established in terms of the components of the energy release rate and fracture toughness. It is supposed that, when the energy release rate, $G$, exceeds the critical value and the critical energy release rate, $G_C$, delamination grows.

Damage initiation is related to the interfacial strength, $\sigma_m$, i.e., the maximum traction on the traction-displacement jump relation. When $v_o$ is reached, the stress is equal to the interfacial tensile strength $\sigma_m$, the maximum stress level possible. For higher relative displacements, the interface accumulates damage and its ability to sustain stress decreases progressively. Once $v$ exceeds $v_f$, the interface is fully debonded and it is no longer able to support any stress. If the load were removed after $v_o$ has been exceeded but before $v_f$ has been reached, the model would unload to the origin. The slope of the constitutive equation before damage initiation, $K_0$, is referred to as the interface stiffness [2, 13].

In the present model, a new parameter $D$ is introduced in order to signify the damage accumulated at the interface:

$$\sigma(v)=[1-D(v)]\,K_0 v \quad (9)$$

where $D$ is a damage parameter, whose initial value is 0. $D$ starts growing when $v>v_o$ and reaches the value when $v>v_f$. Thus, the damage parameter can be computed with the following relations [2]:

$$D(v)=\begin{cases}0 & v\le v_0\\ \dfrac{v_f(v-v_0)}{v(v_f-v_0)} & \text{if } v_0<v\le v_f\\ 1 & v>v_f\end{cases} \quad (10)$$

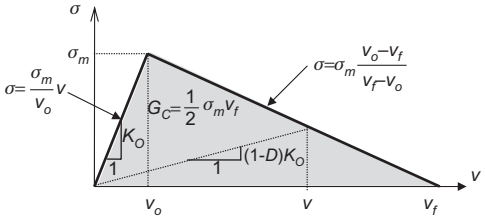



**Figure 2** Bilinear interface traction for Mode I delamination.

As illustrated in Figure 2, the shaded area under the $\sigma$-$v$ curve is the energy dissipated per unit area $G$ for a particular mode; when $v=v_f$, the area of the whole triangle is the critical energy dissipated per unit area $G_C$. $G_C$ is defined as the critical strain energy release rate. In this case, cohesive zone approaches can be related to Griffith's theory of fracture. Furthermore, a perfectly brittle fracture can be simulated when $v_o=v_f$ [2, 11]. The fracture toughness $G_C$, which is the energy required to produce traction-free surfaces, equals the area under the traction-separation curve:

$$G_C=\int_0^{v_f}\sigma \mathrm{d}v=\frac{1}{2}v_f\sigma_m \tag{11}$$

$$v_o=\frac{\sigma_m}{K_O} \tag{12}$$

$v_3^0$ and $v_3^f$ are, respectively, the displacement jumps (Figures 2 and 3) corresponding to delamination onset in mode I and in shear mode:

$$v_3^0=\frac{N_3^0}{K};\quad v_3^f=\frac{N_3^f}{K} \tag{13}$$

where $N_3^0$ and $N_3^f$ are the mode interlaminar strengths. In relation to Figure 2, the opening values $v_i$ are determined by equating the area under the curve to the critical fracture energies such that

$$v_3^f=\frac{2G_{IC}}{K}. \tag{14}$$

The work done per unit area upon complete interface degradation is given by the integration of cohesive tractions as functions of the displacement jump,

$$G_{IC}=\int_0^{v_3^f}\sigma_{33}\mathrm{d}v_3 \tag{15}$$

where $\sigma_{33}$ is the mode traction and $v_3^f$ is the final relative displacements, corresponding to complete decohesion. When the area under the traction-displacement jump relation is equal to the fracture toughness, the traction is reduced to zero and new crack surfaces are formed. The failure criteria for mode I delamination are defined as follows:

$$\frac{G_I}{G_{IC}}=1 \tag{16}$$

The stress-relative displacement relationship can be formulated as [2]:

$$\tau=\begin{bmatrix}\tau_x\\ \tau_y\end{bmatrix}=\begin{bmatrix}K_x(v_x,v_y) & 0\\ 0 & K_y(v_x,v_y)\end{bmatrix}\begin{bmatrix}v_x\\ v_y\end{bmatrix} \tag{17}$$

$$\tau=\begin{bmatrix}(1-D_x(v_x,v_y))K_{ox} & 0\\ 0 & (1-D_y(v_x,v_y))K_{oy}\end{bmatrix}\begin{bmatrix}v_x\\ v_y\end{bmatrix} \tag{18}$$

If a given loading mode has reached 1, the damage variable corresponding to the other loading mode is set as well to 1 to prevent the material from still being able to carry tractions. The displacement jump can then be expressed as [2]:

$$v=\begin{bmatrix}v_x\\ v_y\end{bmatrix}=\begin{bmatrix}\phi_{1c}U_1-\phi_{2c}U_2\\ \phi_{1c}V_1-\phi_{2c}V_2\end{bmatrix} \tag{19}$$

$$\begin{bmatrix}\phi_{1c} & 0 & \phi_{2c} & 0\\ 0 & \phi_{1c} & 0 & \phi_{2c}\end{bmatrix}\begin{bmatrix}U_1\\ V_1\\ U_2\\ V_2\end{bmatrix}=\Phi R \tag{20}$$

where $\Phi$ is the shape functions belonging to sub-domain $\Omega_1$ and $\Omega_2$:

$$\Phi=\begin{bmatrix}\phi_{1c} & 0 & \phi_{2c} & 0\\ 0 & \phi_{1c} & 0 & \phi_{2c}\end{bmatrix} \tag{21}$$

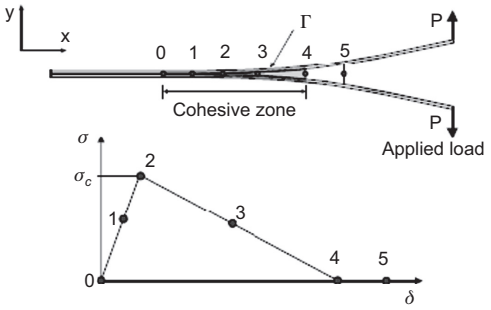



**Figure 3** Cohesive zone ahead of the delamination tip.

# 4 Variational principle

The Galerkin weak form is formulated in a general manner, making use of Lagrange multipliers. It is considered the two-dimensional problem with small displacements on the domain $\Omega$ bounded by $\Gamma$. In the space coordinates $x=[x, y]$, the equilibrium equation is [2, 20]:

$$L^T\sigma+b=0 \quad \text{in} \quad \Omega \tag{22}$$

where $\sigma$ is the stress tensor, which corresponds to the displacement field $u$, and $b$ is the body force vector. The boundary conditions are written as follows:

$$\boldsymbol{\sigma}\cdot\mathbf{n}_t=\bar{t} \text{ on } \Gamma_t \tag{23}$$

$$\boldsymbol{\sigma}\cdot\mathbf{n}_c=\tau(v) \text{ on } \Gamma_c \tag{24}$$

$$u=\bar{u} \text{ on } \Gamma_u \tag{25}$$

where the superposed bar states the prescribed boundary values and **n** is the unit normal to the domain Ω. In addition, $\bar{t}$ and $\bar{u}$ are defined as traction on the traction (natural) boundaries and as displacement on the displacement (essential) boundaries, respectively. $\mathbf{n}_t$ is the normal unity vector of the boundary $\Gamma_t$ where the traction $\bar{t}$ is prescribed, $\mathbf{n}_c$ is the normal unity vector of the boundary $\Gamma_c$ where the traction $\tau(v)$ is prescribed, and $\Gamma_u$ is the boundary where the displacement $\bar{u}$ is imposed.

Since the MLS shape functions are non-interpolating, the Lagrange multipliers are necessary for the EFGM formulation. The weak form is written with Lagrange multipliers, with essential boundary conditions [4]:

$$\begin{aligned}&\int_{\Omega_1}\delta(Lu)^{\mathrm{T}}D(Lu)d\Omega_1+\int_{\Omega_2}\delta(Lu)^{\mathrm{T}}D(Lu)d\Omega_2\\&-\int_{\Omega_1}\delta u^{\mathrm{T}}bd\Omega_1-\int_{\Omega_2}\delta u^{\mathrm{T}}bd\Omega_2-\int_{\Gamma_{t_1}}\delta u^{\mathrm{T}}\bar{t}d\Gamma_{t_1}\\&-\int_{\Gamma_{t_2}}\delta u^{\mathrm{T}}\bar{t}d\Gamma_{t_2}-\int_{\Gamma_c}\delta v^{\mathrm{T}}\tau d\Gamma_c-\int_{\Gamma_{u_1}}\delta\lambda^{\mathrm{T}}(u-\bar{u})d\Gamma_1\\&-\int_{\Gamma_{u_1}}\delta u^{\mathrm{T}}\lambda d\Gamma_1-\int_{\Gamma_{u_2}}\delta\lambda^{\mathrm{T}}(u-\bar{u})d\Gamma_2-\int_{\Gamma_{u_2}}\delta u\lambda^{\mathrm{T}}\lambda d\Gamma_2=0\end{aligned} \tag{26}$$

The weak form is integrated numerically over the domain, taking a sufficiently high order of quadrature, as a function of the size of the background cells and the nodal distribution.

Λ is a vector that collects the nodal Lagrange multipliers for all field nodes on essential boundaries:

$$\Lambda=\sum_{I}^{n_\lambda}\lambda_I^T \tag{27}$$

If we rewrite Eq. (26), by defining **K** and **F** as the global stiffness matrix and the global force vector, respectively [4]:

$$\begin{aligned}&\delta U_1^{\mathrm{T}}\left[K_1U_1+G_1\Lambda_1-F_1\right]+\delta\Lambda_1^{\mathrm{T}}\left[G_1U_1-Q_1\right]\\&+\delta U_2^{\mathrm{T}}\left[K_2U_2+G_2\Lambda_2-F_2\right]\\&+\delta\Lambda_2^{\mathrm{T}}\left[G_2^TU_2-Q_2\right]-\delta U^{\mathrm{T}}K\delta U=0\end{aligned} \tag{28}$$

where **K** is called the nodal stiffness matrix and is defined by the following equation [4]:

$$K_{IJ}=\int_{\Omega_1}(B_I^{\mathrm{T}})_{2\times3}D_{3\times3}(B_J^{\mathrm{T}})_{3\times2}\mathrm{d}\Omega_1+\int_{\Omega_2}(B_I^{\mathrm{T}})_{2\times3}D_{3\times3}(B_J^{\mathrm{T}})_{3\times2}\mathrm{d}\Omega_2 \tag{29}$$

in delaminated part:

$$K^\delta=\Phi^TK(\nu_x,\nu_y)=\begin{bmatrix}\phi_{1c}&0\\0&\phi_{1c}\\\phi_{2c}&0\\0&\phi_{2c}\end{bmatrix}\times\begin{bmatrix}K_x(\nu_x,\nu_y)&0\\0&K_y(\nu_x,\nu_y)\end{bmatrix} \tag{30}$$

$$=\begin{bmatrix}\phi_{1c}K_x(\nu_x,\nu_y)&0\\0&\phi_{1c}K_y(\nu_x,\nu_y)\\\phi_{2c}K_x(\nu_x,\nu_y)&0\\0&\phi_{2c}K_y(\nu_x,\nu_y)\end{bmatrix} \tag{31}$$

Global force **F** is defined as [4]:

$$F=F^b+F^t \tag{32}$$

$$F_i^b=\int_{\Omega_1}\Phi_I^{\mathrm{T}}bd\Omega_1+\int_{\Omega_2}\Phi_I^{\mathrm{T}}bd\Omega_2 \tag{33}$$

and

$$F_i^t=\int_{\Omega_1}\Phi_I^{\mathrm{T}}\bar{t}d\Gamma_{t_1}+\int_{\Omega_2}\Phi_I^{\mathrm{T}}\bar{t}d\Gamma_{t_2} \tag{34}$$

Since both δ$U$ and δΛ are arbitrary, this equation can be satisfied only if [4]:

$$\begin{cases}K_1U_1+K_2U_2+G_1\Lambda_1+G_2\Lambda_2-F_1-F_2+K^\delta U=0\\G_1^TU_1+G_2^TU_2-Q_1-Q_2=0\end{cases} \tag{35}$$

Eq. (35) can be rewritten in matrix form as follows [4]:

$$\begin{bmatrix}K_1+k^\delta&G_1&0&0\\G_1^T&0&0&0\\0&0&K_2+k^\delta&G_2\\0&0&G_2^T&0\end{bmatrix}\begin{Bmatrix}U_1+U\\\Lambda_1\\U_2+U\\\Lambda_2\end{Bmatrix}=\begin{Bmatrix}F_1\\Q_1\\F_2\\Q_2\end{Bmatrix} \tag{36}$$

then the solution to the whole problem can be obtained by the iterative solution of Eq. (36).

In the conventional EFGM, the stiffness matrix, Eq. (29), and load factor, Eq. (36), are computed by the Gaussian quadrature method with a background mesh.

**Q** and **G** are defined as the global vector form and global matrix form, respectively [4]:

$$Q_I^{\mathrm{T}}=-\int_{\Gamma_u}N_I^{\mathrm{T}}\bar{u}\mathrm{d}\Gamma \tag{37}$$

$$G_{IJ}^{\mathrm{T}}=-\int_{\Gamma_u}N_I^{\mathrm{T}}\Omega_J\mathrm{d}\Gamma \tag{38}$$

To illustrate the applicability of the meshfree method, the delamination under mode I loading is simulated.

# 5 Numerical implementation: delamination of composite specimens

To demonstrate the usefulness of the proposed method, the delamination problem is analyzed by the EFGM. Linear

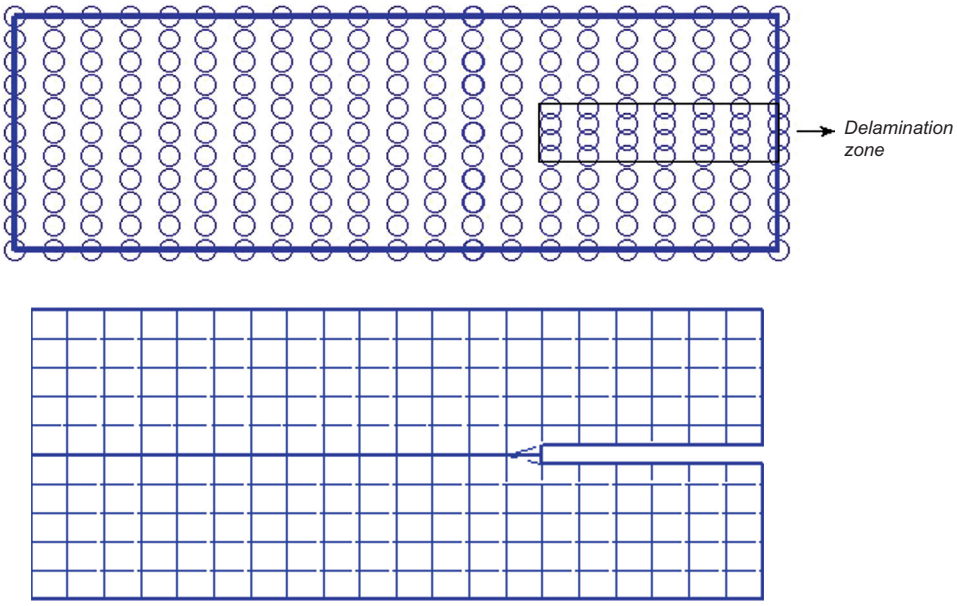



**Figure 4** Background meshes of integration cells for the EFGM.

basis functions in two dimensions are used. In addition, the cubic spline is taken as a weight function. The number of cells was 200 (20×10) (Figure 4) [23].

The codes calculating the critical load and energy release rate were developed in MATLAB for mode I testing of a delaminated composite for various orientation angles and materials [23]. The analysis was performed for $[0]_{10}$, $[0/45/-45/90/0]_s$, $[0/90/0/90/0]_s$, $[0/90/0/90/30]_s$, $[0/90/0/90/45]_s$, and $[0/90/0/90/60]_s$ laminates with mid-plane delaminations, and the results were verified for different composite materials: E-glass/epoxy, S-glass/epoxy, Kevlar/epoxy (Aramid149/epoxy), carbon/epoxy (AS4/3501-6), carbon/PEEK (AS4/APC2), and carbon/epoxy (IM6/SC1081). As an example, a load-energy release rate diagram is shown in Figure 5 for the $[0/45/-45/90/0]_s$ Kevlar/epoxy laminate (Aramid 149/epoxy).

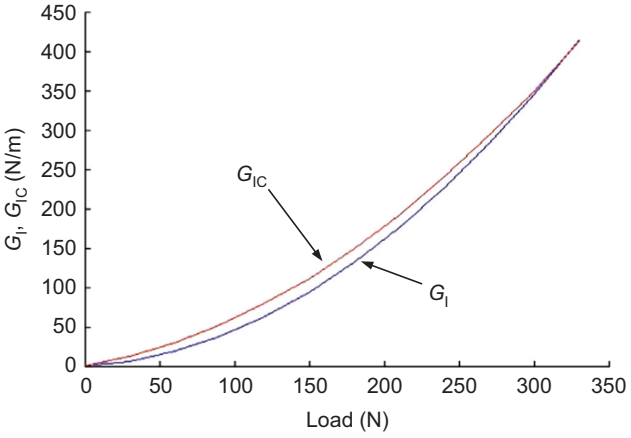



**Figure 5** Energy release rate load diagram obtained from the meshfree method for the $[0/45/-45/90/0]_s$ Kevlar/epoxy laminate.

As shown in Figure 5, the critical load and energy release rate obtained were 322 N and 395.84 N/m, respectively.

In addition, values of the integral for 219 (11×19) and 231 (11×21) background nodes with equivalent interval sizes were compared. In Table 2, the critical loads are shown for carbon/epoxy with $[0]_{10}$ stacking sequence. For a relatively fine background meshes, the critical load was converged.

The analyses were also done with the finite element method which accounts for the contact between delaminated layers and fracture mode separation where the crack propagation was simulated with a moving mesh scheme. Finite element analysis was carried out using the ANSYS software. To conform to the geometry and material behavior for each of the undelaminated and delaminated layers, the 4-node SOLID-182 and cohesive INTER 202 elements were selected, respectively. In the analysis, a total of 1347 nodes and 940 elements were used.

A plot of the reaction force as a function of the applied end displacement for the Kevlar/epoxy specimen (Aramid 149/epoxy) is shown in Figure 6.

**Table 2** Comparison of the meshfree method results for the carbon/epoxy laminate with $[0]_{10}$.

| Nodes | Critical load (N) |
|---|---|
| 11×19 | 128 |
| 11×21 | 186 |

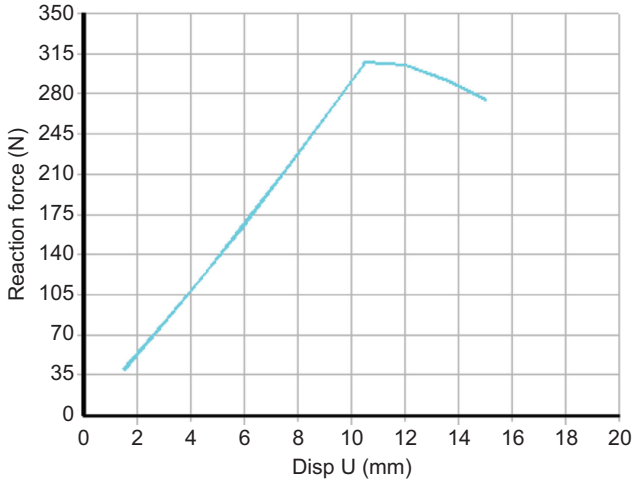



**Figure 6** Force vs. displacement result of finite element analysis.

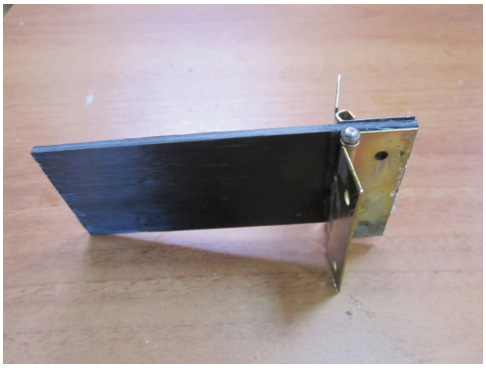


**Figure 7** Specimen for DCB test.

## 6 Comparisons with experimental studies

The DCB mode I fracture specimen (ASTM D5528) was employed to characterize the delamination resistance. The specimen thicknesses were sized based on the desire to obtain a small deflection (linear elastic load-displacement response).

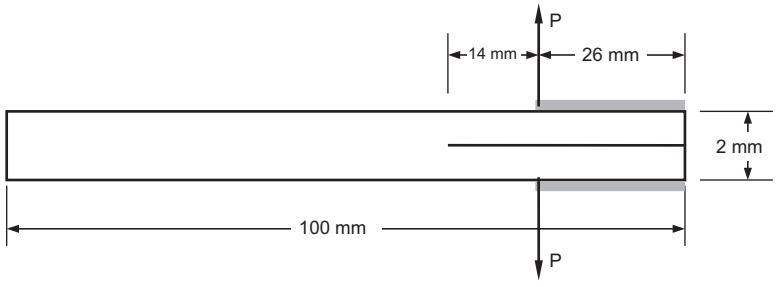



**Figure 8** Specimen dimensions.

The experiment was carried out for $[0]_{10}$ and $[0/90/0/90/0]_s$ carbon/epoxy (AS4/3501-6) specimens with mid-plane delaminations (Figure 7).

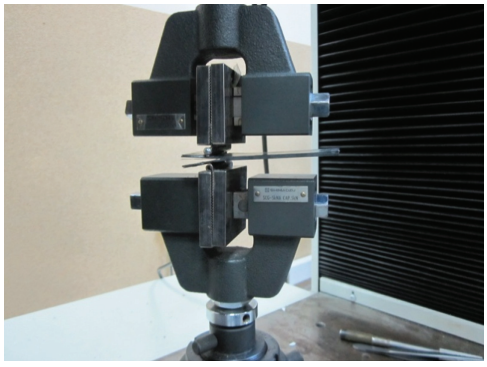


**Figure 9** DCB specimen for mode I testing mounted on the fixture.

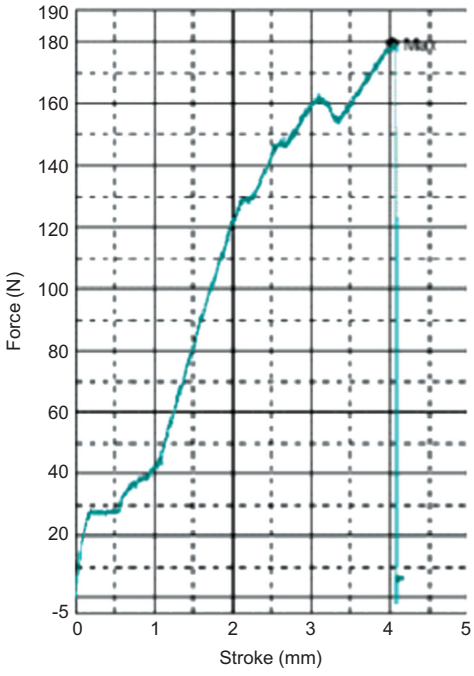



**Figure 10** Load-displacement curve for the $[0]_{10}$ carbon/epoxy laminate in the DCB test.

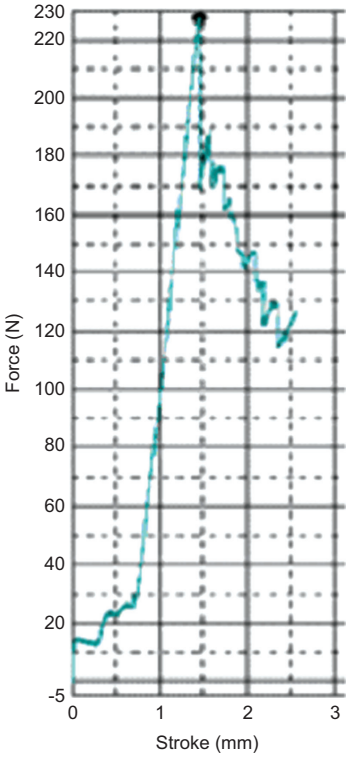



**Figure 11** Load-displacement curve for the $[0/90/0/90/0]_s$ carbon/epoxy laminate in the DCB test.

**Table 3** Critical load and energy release rate amount for the carbon/epoxy laminate (AS4/3501-6) in mode I testing.

| Orientation angle | P (N) | $G$ (N/m) |
|---|---|---|
| $[0]_{10}$ | 179.50 | 123.95 |
| $[0/90/0/90/0]_s$ | 227.50 | 199.10 |

The laminates were fabricated from carbon/epoxy prepreg. The delamination cracks were simulated by Teflon films. The single ply thickness was 0.2 mm and had the following elastic properties: $E_{11}$=146.7 GPa, $E_{22}$=7.8 GPa, $G_{12}=G_{13}$=4.8 GPa, $\nu_{12}$=0.29 [24].

The DCB test was a pure Mode I crack propagation test. The specifications for the specimen are illustrated in Figure 8, which are as follows: $L$=100 mm, $h$=2 mm, initial crack length =14 mm, and width $b$=40 mm.

Fracture testing was performed using a Shimadzu displacement control test frame having a load cell of 100 kN capacity. The test sample shown in Figure 9 was loaded with a speed of 10 mm/min. The incremental test method for mode I fracture testing which requires the loading-crack propagation-unloading sequence was followed.

Figures 10 and 11 show representative load-displacement (P-δ) curves for $[0]_{10}$ and $[0/90/0/90/0]_s$ of the DCB carbon/epoxy (AS4/3501-6) specimens, respectively. As shown in Figure 11, when the displacement reaches about 1.5 mm, the discontinuity begins to propagate along the horizontal straight line. As the cohesive traction decreases with the increasing separation, the load-displacement curve rapidly declines as the crack propagates.

Data reduction for mode I fracture testing was based on the empirical compliance method proposed by Berry [25], The fracture toughness, $G_{IC}$, associated with each crack length, $a$, is

$$G_{IC}=\frac{nP_c\delta_c}{2ba} \tag{39}$$

where $P_c$ is the critical load, $\delta_c$ is the corresponding critical displacement, and $b$ is the specimen width. $P_c$ was evaluated from the maximum load corresponding to each crack length.

In the present study, the classical Daniel-Ishai expression [26] was utilized to obtain the strain energy release rate from the beam solution, i.e.,

$$G_{IC}=\frac{12P^2}{E_1b^2h}\left[\left(\frac{a}{h}\right)^2+0.1\frac{E_1}{G_{31}}\right] \tag{40}$$

**Table 4** Results of the meshfree and finite element methods (FEMs).

| Orientation angle | $[0]_{10}$ | | | $[0/45/-45/90/0]_s$ | | | $[0/90/0/90/0]_s$ | | |
|---|---|---|---|---|---|---|---|---|---|
| | P (N) | | | P (N) | | | P (N) | | |
| | Meshfree | FEM | Difference | Meshfree | FEM | Difference | Meshfree | FEM | Difference |
| E-glass/epoxy | 19.50 | 19.46 | 0.205 | 28.00 | 26.76 | 4.428 | 22.50 | 21.80 | 3.111 |
| S-glass/epoxy | 22.50 | 21.03 | 6.444 | 28.20 | 27.31 | 3.156 | 21.50 | 21.02 | 2.232 |
| Kevlar/epoxy (Aramid149/epoxy) | 124.00 | 121.41 | 2.088 | 322.00 | 307.08 | 4.634 | 128.00 | 124.66 | 2.609 |
| Carbon/epoxy (AS4/3501-6) | 186.00 | 180.15 | 3.145 | 395.00 | 365.06 | 7.579 | 265.00 | 251.13 | 5.234 |
| Carbon/PEEK (AS4/APC2) | 173.00 | 144.10 | 16.705 | 447.00 | 444.60 | 0.536 | 236.00 | 232.11 | 1.648 |
| Carbon/epoxy (IM6/SC1081) | 271.00 | 269.77 | 0.454 | 785.00 | 783.34 | 0.211 | 397.00 | 389.56 | 1.874 |

$\text{Difference}=\left[\frac{M-FEM}{M}\times 100\right]$.

**Table 5** Results of the meshfree and finite element methods (continuous).

| Orientation angle | $[0/90/0/90/30]_s$ | | | $[0/90/0/90/45]_s$ | | | $[0/90/0/90/60]_s$ | | |
|---|---|---|---|---|---|---|---|---|---|
| | P (N) | | | P (N) | | | P (N) | | |
| | Meshfree | FEM | Difference | Meshfree | FEM | Difference | Meshfree | FEM | Difference |
| E-glass/epoxy | 24.50 | 24.33 | 0.694 | 15.80 | 15.32 | 3.038 | 9.10 | 8.89 | 2.308 |
| S-glass/epoxy | 22.50 | 20.78 | 7.644 | 12.70 | 12.43 | 2.126 | 9.80 | 9.72 | 0.816 |
| Kevlar/epoxy (Aramid149/epoxy) | 97.50 | 93.02 | 4.594 | 39.00 | 36.17 | 7.256 | 15.80 | 14.96 | 5.316 |
| Carbon/epoxy (AS4/3501-6) | 153.00 | 143.73 | 6.059 | 49.00 | 44.80 | 8.571 | 27.20 | 25.68 | 5.588 |
| Carbon/PEEK (AS4/APC2) | 142.00 | 139.08 | 2.056 | 45.30 | 44.08 | 2.693 | 24.50 | 23.96 | 2.204 |
| Carbon/epoxy (IM6/SC1081) | 221.00 | 214.42 | 2.977 | 63.00 | 62.68 | 0.507 | 28.90 | 26.32 | 8.927 |

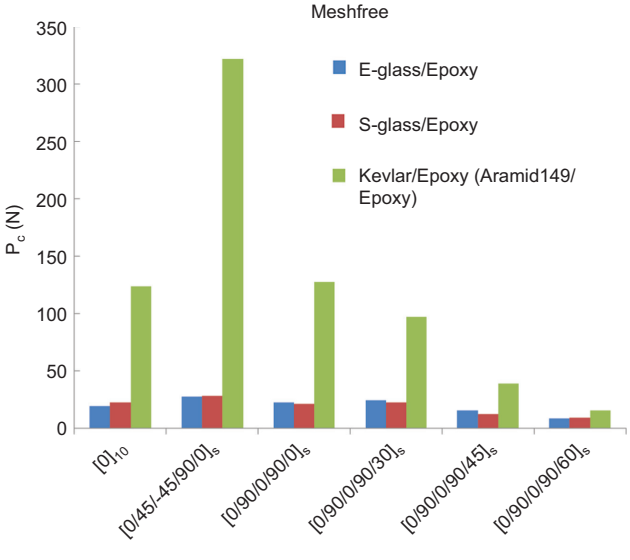



**Figure 12** Critical loads for various orientation angles.

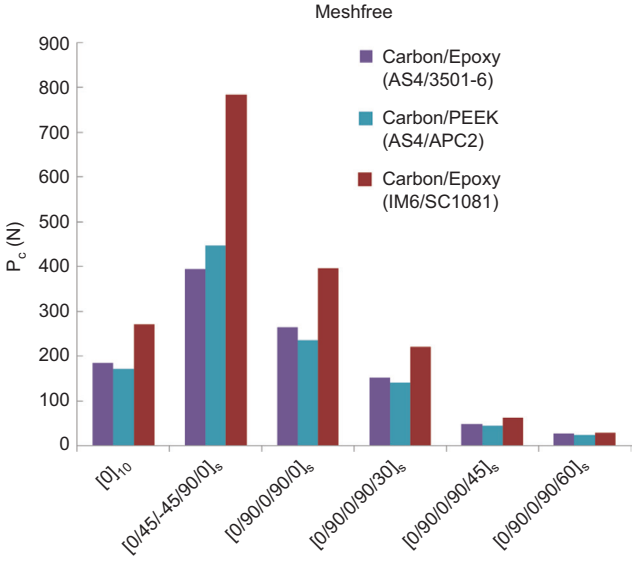



**Figure 13** Critical loads for various orientation angles (continuous).

In Eq. (40), $P$ is the critical applied load, $b$ is the specimen width, $a$ is the crack length, $h$ is the specimen thickness, and $E_1$ and $G_{31}$ are the elastic modulus throughout the fiber direction and the shear modulus of composite materials, respectively.

Firstly, the critical load was experimentally obtained. Then, the strain energy release rate $G_{1c}$ given in Eq. (39) was calculated. Table 3 shows the critical load and energy release rate for carbon/epoxy laminate (AS4/3501-6) for mode I loading.

## 7 Results and discussion

In this paper, the critical load and energy release rate for mode I testing of a delaminated composite for various orientation angles and materials were obtained and compared. In the experimental method, the DCB specimen was used. The obtained results from the experimental method are supported by the meshfree and finite element numerical methods.

The critical loads obtained from the meshfree and finite element methods for various composite specimens and different orientation angles are given in Tables 4 and Table 5. As shown in Tables 4 and 5, the results obtained by the EFGM are very close to the results obtained by the finite element method. It is also shown that the largest critical load and energy release rate are obtained for carbon/epoxy (IM6/SC1081) specimen with $[0/45/-45/90/0]_s$ orientation angle (Figures 12–15).

The critical loads for various composite materials and orientation angle are shown in Figures 12 and 13.

As shown in Figures 12 and 13 for the same composite material and $[0/45/-45/90/0]_s$, $[0/90/0/90/0]_s$, $[0]_{10}$, $[0/90/0/90/30]_s$, $[0/90/0/90/45]_s$, and $[0/90/0/90/60]_s$

**Table 6** Comparison of the critical loads for carbon/epoxy laminate (AS4/3501-6) in mode I.

| Orientation angle | $D/A_{22}$ (m²) | Experimental | Meshfree | Difference $\left[\frac{E-M}{E}\times 100\right]$ | Finite element | Difference $\left[\frac{E-FEM}{E}\times 100\right]$ |
|---|---|---|---|---|---|---|
| $[0]_{10}$ | 2.21E-07 | 179.50 | 186.00 | -3.62 | 180.15 | -0.362 |
| $[0/90/0/90/0]_s$ | 2.23E-07 | 227.50 | 265.00 | -16.48 | 251.13 | -10.39 |

**Table 7** Comparison of $D/A_{22}$ (m²) and the critical loads for carbon/epoxy laminate (AS4/3501-6) in mode I.

| Orientation angle | $D/A_{22}^{-1}$ (m²)×10⁻⁷ | Critical load (N) (meshfree method) |
|---|---|---|
| $[0]_{10}$ | 2.21 | 186 |
| $[0/45/-45/90/0]_s$ | 2.51 | 395 |
| $[0/90/0/90/0]_s$ | 2.23 | 265 |
| $[0/90/0/90/30]_s$ | 2.20 | 153 |
| $[0/90/0/90/45]_s$ | 2.15 | 49 |
| $[0/90/0/90/60]_s$ | 2.05 | 27.2 |

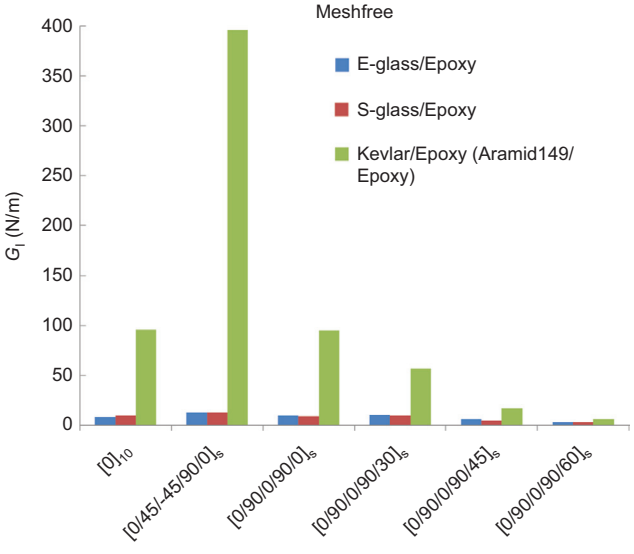



**Figure 14** Energy release rates for various orientation angles.

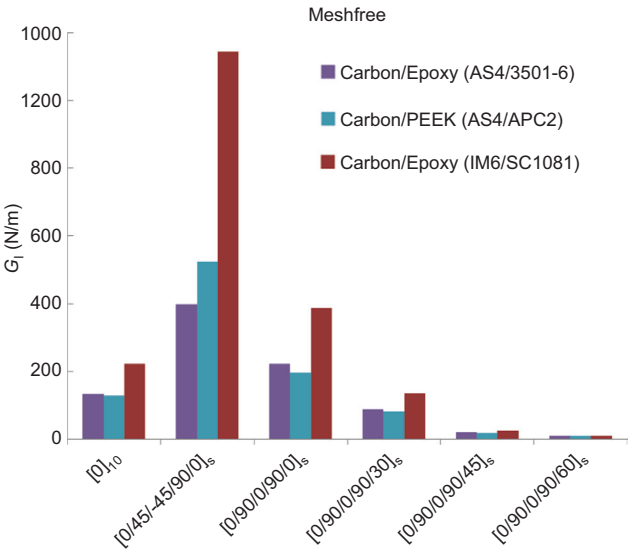



**Figure 15** Energy release rates for various orientation angles (continuous).

orientation angles, critical loads are reduced due to the amounts of $D/A_{22}$ are reduced in order (Tables 6 and 7). Consequently, according to Eq. (15) the amounts of energy release rate are reduced (Figures 14 and 15).

# 8 Conclusions

In this paper, the numerical and experimental investigation analysis of delamination problem under mode I loading in composite materials are presented. Based upon the results of this study, the following conclusions can be drawn:

- Results obtained from the meshfree method showed very good agreement with experimental evidences for single-mode delamination under mode I loading. Therefore, the meshfree method is capable of accurately predicting delamination growth.
- In the meshfree method, critical loads and energy release rates are increased by increasing the number of nodes. That is because the node density is increased everywhere including in the crack tip region. A relatively fine background mesh helps the analysis to estimate the critical load and energy release rate. Although the uniform mesh density was used in the analysis, for better performance varying the node density can be done such that more nodes may be placed around the crack tip while fewer nodes are used in the other regions.
- Results obtained from numerical methods and experimental tests showed that critical energy release rate is directly related to interlaminar tensile strength.
- The maximum and the minimum critical loads and energy release rates occurred for the $[0/45/-45/90/0]_s$

and $[0/90/0/90/60]_s$ orientation angles, respectively (Table 7). Since Mode I energy release rate is calculated by using Eq. (15), whereas out-of-plane stress is calculated as

$$\sigma_y = DA_{22}^{-1}N_y \tag{41}$$

- the value of the expression $D/A_{22}$ affects the critical load and energy release rate values directly.
- Comparison of the critical loads of two ply orientations and one material obtained from both methods with the experiments (Table 6) showed that the results of the finite element analyses are closer to the experiments than to the meshfree results. This may be the result of the mesh (node) number difference in the numerical analyses. The total number of elements in the meshes and in the finite element methods is not equal to each other. While a total of 1347 nodes and 940 elements were used in the finite element analysis, 200 cells and 231 nodes were used in the meshes. An equivalent mesh-cell comparison might give more reasonable and meaningful results.

Consequently, the meshfree method could also be used effectively to study delamination growth in composite laminates and is especially suitable for the simulation of complex delamination patterns that are difficult to model using other numerical methods.

## Appendix: Analysis of laminated beams using the CLPT

Consider the bending of symmetrically laminated beams according to the classical laminated plate theory (CLPT). For symmetric laminates, the equations for bending deflection are uncoupled from those of stretching displacements. $b$ and $h$ are defined as the width and the total thickness of the laminate, respectively. $M_{xx}$, $M_{yy}$, and $M_{xy}$ are defined as the bending moments per unit of length of the plate [25–31].

In deriving the laminated beam theory, we assume that:

$$M_{yy} = M_{xy} = 0 \tag{A.1}$$

The classical laminated plate theory constitutive equations for symmetric laminates, in the absence of in-plane forces, are given by:

$$\begin{Bmatrix} M_{xx} \\ M_{yy} \\ M_{xy} \end{Bmatrix} = -\begin{bmatrix} D_{11} & D_{12} & D_{16} \\ D_{12} & D_{22} & D_{26} \\ D_{16} & D_{26} & D_{66} \end{bmatrix} \begin{Bmatrix} \dfrac{\partial^2 w_0}{\partial x^2} \\ \dfrac{\partial^2 w_0}{\partial y^2} \\ 2\dfrac{\partial^2 w_0}{\partial x \partial y} \end{Bmatrix} \tag{A.2}$$

In the beam theory, we assume that the laminated beam under consideration is long enough to make the effect of the Poisson ratio and shear coupling on the deflection negligible. Then the transverse deflection can be treated only as a function of coordinate $x$ and time $t$:

$$w_0 = w_0(x, t) \tag{A.3}$$

Then we can write:

$$\frac{\partial^2 w_0}{\partial x^2} = -D_{11}^* M_{xx} \tag{A.4}$$

The in-plane stress in the $k$th layer can be obtained from:

$$\begin{aligned} \sigma_{xx}^{(k)}(x,z) &= \frac{M(x)z}{b}\left(Q_{xx}^{(k)}D_{11}^* + Q_{xy}^{(k)}D_{12}^* + Q_{xs}^{(k)}D_{16}^*\right) \\ \sigma_{xy}^{(k)}(x,z) &= \frac{M(x)z}{b}\left(Q_{xy}^{(k)}D_{11}^* + Q_{yy}^{(k)}D_{12}^* + Q_{ys}^{(k)}D_{16}^*\right) \\ \sigma_{xy}^{(k)}(x,z) &= \frac{M(x)z}{b}\left(Q_{xs}^{(k)}D_{11}^* + Q_{ys}^{(k)}D_{12}^* + Q_{ss}^{(k)}D_{16}^*\right) \end{aligned} \tag{A.5}$$

Where

$$\begin{aligned} D_1 &= D_{22}D_{66} - D_{26}D_{26} \\ D_2 &= D_{16}D_{26} - D_{12}D_{66} \\ D_3 &= D_{12}D_{26} - D_{22}D_{16} \\ D^* &= D_{11}D_1 + D_{12}D_2 + D_{16}D_3 \\ D_{11}^* &= D_1 / D^* \\ D_{12}^* &= D_2 / D^* \\ D_{16}^* &= D_3 / D^* \end{aligned} \tag{A.6}$$

Interlaminar stresses may be computed using the equilibrium equations of three-dimensional elasticity for each layer; these equations may be integrated with respect to $z$ to obtain the interlaminar stresses within each layer.

$$\begin{aligned} \sigma_{xz}^{(k)} &= -\int_{z_k}^{z}\left(\frac{\partial \sigma_{xx}^{(k)}}{\partial x} + \frac{\partial \sigma_{xy}^{(k)}}{\partial y}\right)dz + G^{(k)} \\ \sigma_{yz}^{(k)} &= -\int_{z_k}^{z}\left(\frac{\partial \sigma_{xy}^{(k)}}{\partial x} + \frac{\partial \sigma_{yy}^{(k)}}{\partial y}\right)dz + F^{(k)} \\ \sigma_{zz}^{(k)} &= -\int_{z_k}^{z}\left(\frac{\partial \sigma_{xz}^{(k)}}{\partial x} + \frac{\partial \sigma_{yz}^{(k)}}{\partial y}\right)dz + H^{(k)} \end{aligned} \tag{A.7}$$

Derivatives with respect to $y$ are zero since all variables are independent of $y$ for beams.

$$\sigma_{xz}^{(k)} = -Q_x(x)\left(Q_{xx}^{(k)}D_{11}^{*} + Q_{xy}^{(k)}D_{12}^{*} + Q_{xs}^{(k)}D_{16}^{*}\right)\left(\frac{z^2 - z_k^2}{2}\right) + G^{(k)}$$
$$\sigma_{zz}^{(k)} = -\frac{dQ_z}{dx}\left(Q_{xx}^{(k)}D_{11}^{*} + Q_{xy}^{(k)}D_{12}^{*} + Q_{xs}^{(k)}D_{16}^{*}\right)\left(\frac{z^3 - z_k^3}{6}\right) + H^{(k)} \quad \text{(A.8)}$$

If we consider $G(1)=0$ and $H(1)=0$, then we have:

$$G^{(k+1)} = -Q_x(x)\left(Q_{xx}^{(k)}D_{11}^{*} + Q_{xy}^{(k)}D_{12}^{*} + Q_{xs}^{(k)}D_{16}^{*}\right)\left(\frac{z^2 - z_k^2}{2}\right) + G^{(k)}$$
$$H^{(k+1)} = -\frac{dQ_z}{dx}\left(Q_{xx}^{(k)}D_{11}^{*} + Q_{xy}^{(k)}D_{12}^{*} + Q_{xs}^{(k)}D_{16}^{*}\right)\left(\frac{z^2 - z_k^3}{2}\right) + H^{(k)} \quad \text{(A.9)}$$

Considering the point load at the free end, deflection is defined as follows:

$$w_0(x) = \frac{F_0 b a^3}{6E_{xx}^{b} I_{yy}}\left[3\left(\frac{x}{a}\right)^2 - \left(\frac{x}{a}\right)^3\right] \quad \text{(A.10)}$$

The normal stress in the $z$ direction is zero and the shear stress on the cross section is written as:

$$\sigma_{xz}^{(k)} = -\frac{F_0 b}{E_{xx}^{b} I_{yy} D_{11}^{*}}\left(Q_{xx}^{(k)}D_{11}^{*} + Q_{xy}^{(k)}D_{12}^{*} + Q_{xs}^{(k)}D_{16}^{*}\right)\left(\frac{z^2 - z_K^2}{2}\right) + G^{(k)} \quad \text{(A.11)}$$

Finally, the normal stress obtained from Eq. (A.1) is used to calculate the energy release rate (). $\int_{.0}^{v_3^f} \sigma_{33} dv_3 = G_{IC}$.

Received January 23, 2013; accepted May 8, 2013; previously published online June 21, 2013

# References


[1] Turon A, Camanho PP, Costa J, Dávila CG. *Mech. Mat.* 2006, 38, 1072–1089.
[2] Barbieri E, Meo M. *Compos. Sci. Tech.* 2009, 69, 2169–2177.
[3] Fries TP, Matthies HG. Technical University Braunschweig Brunswick, Informatikbericht 2003-3, Germany 2004.
[4] Liu GR. *Mesh Free Methods Moving Beyond the Finite Element Method*, CRC Press: New York, 2003.
[5] Liu GR, Gu YT. *An Introduction to Meshfree Methods and Their Programming*, Springer: Netherlands, 2005.
[6] Rajendran S, Song DQ. *Proceedings of 2nd Asian ANSYS User Conference*, Singapore, Nov. 11–13, 1998.
[7] Camanho PP, Dávila CG, Ambur DR. NASA/TP-211041, 2001.
[8] Camanho PP, Dávila CG, De Moura MF. NASA Langley Research Center: Hampton, 2003, VA23681-2199.
[9] Li S, Liu WK. *ASME App. Mech. Rev.* 2002, 55, 1–34.
[10] Pantano A, Averill RC. *Int. J. Solids Struct.* 2004, 41, 3809–3831.
[11] De Borst R, Remmers JJC. *Comp Sci. Tech.* 2006, 66, 713–722.
[12] Yuzhou S, Hu YG, Liew KM. *Int. J. Eng. Sci.* 2007, 45, 541–553.
[13] Turon A, Dávila CG, Camanho PP, Costa J. *Eng. Fracture Mech.* 2007, 74, 1665–1682.
[14] Samborsky DD, Wilson TJ. *J. Solar Energ. Eng.* 2008, 130.
[15] Guiamatsia I, Falzon BG, Davies GAO. *Key Eng. Mater.* 2008, 383, 53–66.
[16] Guiamatsia I, Falzon BG, Davies GAO, Iannucci L. *Comp. Sci. Tech.* 2009, 69, 2640–2648.
[17] Liew KM, Zhao X, Ferreira AJM. *Comp Struct.* 2011, 93, 2031–2041.
[18] Pekedis M. *Ağsız yöntemlerle yapısal analiz*, Master Thesis (In Turkish), Ege University, Department of Mechanical Engineering: Izmir, 2009.
[19] Sosa JLC, Karapurath N. *Comp. Sci. Tech.* 2012, 72, 788–791.
[20] Belytschko T, Gu L, Lu YY. *Model. Simu. Mat. Sci. Eng.* 1994, 519–534.
[21] Belytschko T, Krongauz Y, Organ D, Fleming M, Krysl P. *Comput. Methods Appl. Mech. Eng.* 1996,139, 3–47.
[22] Most T, Bucher C. *Eng. Anal. Boundary Elem.* 2008, 32, 461–470.
[23] Hesar GG. *Kompozit Malzemelerde Delaminasyon Davranışının Ağsız Yöntemler ile Analizi*, Master Thesis (In Turkish), Ege University, Department of Mechanical Engineering: Izmir, 2012.
[24] Yılmaz B. *Karbon Fiber Kompozit Ayak Protezi Tasarım ve İmalatı*, Master Thesis (In Turkish), Ege University, Department of Mechanical Engineering: Izmir, 2009.
[25] Berry JP. *J. App. Phy.* 1963, 34, 62–68.
[26] Isaac MD, Ishai O. *Engineering Mechanics of Composite Materials*, Oxford University Press: New York, 1994.
[27] Adams DF, Carlsson LA, Pipes RB. *Experimental Characterization of Advanced Composite Materials*, 3rd ed., CRC Press: New York, 2003.
[28] Kollar LP. *Mechanics of Composite Structures*, Cambridge University Press: New York, 2003.
[29] Reddy JN. *Mechanics of Laminated Composite Plates and Shells Theory and Analysis*, 2nd ed., CRC Press: New York, 2004.
[30] Kaw AK. *Mechanics of Composite Materials*, 2nd ed., CRC Press: New York, 2006.
[31] Sridharan S. *Delamination Behaviour of Composite*, CRC Press, Cambridge: England, 2008.